fractal and fractional

MDPI

Article

A High-Performance Fractional Order Controller Based on Chaotic Manta-Ray Foraging and Artificial Ecosystem-Based Optimization Algorithms Applied to Dual Active Bridge Converter

Felipe Ruiz [1,*], Eduardo Pichardo [2], Mokhtar Aly [1], Eduardo Vazquez [3], Juan G. Avalos [3] and Giovanny Sánchez [3,*]

[1] Facultad de Ingeniería, Arquitectura y Diseño, Universidad San Sebastián, Bellavista 7, Santiago 8420524, Chile; mokhtar.aly@uss.cl
[2] Tecnologico de Monterrey, School of Engineering and Sciences, Calle del Puente 222, Col. Ejidos de Huipulco Tlalpan, Ciudad de Mexico 14380, Mexico; epichardom@tec.mx
[3] Instituto Politécnico Nacional, ESIME Culhuacan, Av. Santa Ana No. 1000, Ciudad de Mexico 04260, Mexico; edvazquezf@ipn.mx (E.V.); javaloso@ipn.mx (J.G.A.)
* Correspondence: felipe.ruiz@uss.cl (F.R.); gsanchezriv@ipn.mx (G.S.); Tel.: +56-9-37082753 (F.R.)

Abstract: Over the last decade, dual active bridge (DAB) converters have become critical components in high-frequency power conversion systems. Recently, intensive efforts have been directed at optimizing DAB converter design and control. In particular, several strategies have been proposed to improve the performance of DAB control systems. For example, fractional-order (FO) control methods have proven potential in several applications since they offer improved controllability, flexibility, and robustness. However, the FO controller design process is critical for industrializing their use. Conventional FO control design methods use frequency domain-based design schemes, which result in complex and impractical designs. In addition, several nonlinear equations need to be solved to determine the optimum parameters. Currently, metaheuristic algorithms are used to design FO controllers due to their effectiveness in improving system performance and their ability to simultaneously tune possible design parameters. Moreover, metaheuristic algorithms do not require precise and detailed knowledge of the controlled system model. In this paper, a hybrid algorithm based on the chaotic artificial ecosystem-based optimization (AEO) and manta-ray foraging optimization (MRFO) algorithms is proposed with the aim of combining the best features of each. Unlike the conventional MRFO method, the newly proposed hybrid AEO-CMRFO algorithm enables the use of chaotic maps and weighting factors. Moreover, the AEO and CMRFO hybridization process enables better convergence performance and the avoidance of local optima. Therefore, superior FO controller performance was achieved compared to traditional control design methods and other studied metaheuristic algorithms. An exhaustive study is provided, and the proposed control method was compared with traditional control methods to verify its advantages and superiority.

Keywords: dual active bridge converter; fractional order controller; metaheuristic algorithms; chaotic manta-ray foraging optimization; artificial ecosystem-based optimization; power electronics

check for updates

Citation: Ruiz, F.; Pichardo, E.; Aly, M.; Vazquez, E.; Avalos, J.G.; Sánchez, G. A High-Performance Fractional Order Controller Based on Chaotic Manta-Ray Foraging and Artificial Ecosystem-Based Optimization Algorithms Applied to Dual Active Bridge Converter. *Fractal Fract.* **2024**, *8*, 332. https://doi.org/10.3390/fractalfract8060332

Academic Editors: Arman Oshnoei and Mahdieh S. Sadabadi

Received: 1 April 2024
Revised: 28 May 2024
Accepted: 28 May 2024
Published: 31 May 2024

Copyright: © 2024 by the authors. Licensee MDPI, Basel, Switzerland. This article is an open access article distributed under the terms and conditions of the Creative Commons Attribution (CC BY) license (https://creativecommons.org/licenses/by/4.0/).

1. Introduction

1.1. Overview

Climate change is a fundamental threat to humanity and planetary health [1]. Moreover, power electronics play a crucial role in achieving a transition towards energy-sustainable development [2]. For this reason, applications such as microgrids [3], electric vehicles [4], energy storage systems [5], and solid-state transformers [6], among others, are under development. In particular, efforts have been dedicated to developing efficient dual active bridge (DAB) converters since these components are a cornerstone of high-frequency isolated DC–DC conversion.

The DAB topology has garnered wide industrial and research interest, and many strategies have been proposed to fully exploit its high power density, bidirectional power flow, galvanic isolation, and soft switching characteristics [7–9]. Obviously, the development of advanced models and control methods leads to improved performance; however, several factors associated with DAB systems, such as nonlinear dynamics and degree of freedom, must be considered. In addition, the design of these systems must consider the DAB's own characteristics, i.e., having a direct current (DC) input and output with an alternating current (AC) in the middle due to the high-frequency transformer (HFT).

1.2. Related Work

In the literature, several models have been proposed to address issues with the DAB topology, such as the reduced-order model, harmonic modeling [10], the generalized average model (GAM) [11], the phasor transformation [12,13], and the discrete-time model [14]. Specifically, the reduced-order model focuses on the low-frequency region. However, these systems have limitations, especially when used in real-time applications, due to the effects of high-frequency regions. In addition, reduced-order models neglect the DC bias current and inductor RMS current. However, these currents should be considered when system efficiency is important. To overcome this issue, the use of GAM approximation is a potential solution because the resulting model provides more physical insight [15]. Therefore, various authors have included GAM approximation in DAB converter structure modeling.

Regarding control improvement, various techniques, such as the proportional-integral (PI) controller or linear quadratic Gaussian (LQG) control, have been used. In addition, the authors of [16] used nonlinear controllers applied to the GAM model. Despite providing significant improvements, these proposals still present limitations in terms of controllability and robustness. In the last two decades, several methods have focused on the development of new schemes to include fractional operators into controllers [17–19]. The developed schemes use fractional-order derivatives and integrals, which potentially improve the performance and robustness of DABs. Specifically, fractional-order (FO) controllers offer lower sensitivity to parametric changes, noise, and transient enhancements [20] compared with conventional integer-order controllers, such as PI and PI-derivative (PID) ones. However, PID controllers can be extended using FO methods. Hence, FO-based PID controllers provide more flexibility than conventional PID control, resulting in more robust designs.

Various methods have been proposed for the design of fractional-order proportional-integral-derivative (FOPID) controllers [21]. For example, in [22], the authors proposed a pole distribution for the characteristic equation in the complex plane. Another approach was presented based on a frequency domain in [23,24]. Moreover, a state-space design method based on feedback pole placement was presented in [25], and another method based on loop shaping using linear matrix inequalities (LMI) was provided in [26]. In general terms, to achieve an efficient design of FO-based PID controllers, parameter optimization represents a significant challenge since the optimal value determines the robustness of the DAB system. Metaheuristic algorithms, which are based on evolutionary computation techniques, have emerged as a potential method to achieve optimal performance [27]. Recently, various authors have proposed hybrid combinations of metaheuristic algorithms. These involve the use of two algorithms with complementary capabilities to improve global performance, i.e., the hybrid combination merges the best properties of each algorithm to mitigate the weaknesses of each [28,29].

1.3. Paper Contribution and Organization

This paper presents a comprehensive analysis and design method to improve FO control-based DABs applied to power electronics applications. The main contributions of this study can be summarized as follows:

- A hybrid combination of two metaheuristic algorithms is proposed for the first time to improve the convergence speed and precision of the FO-based PID controller. The new hybrid algorithm is based on the chaotic artificial ecosystem-based optimization

(AEO) and manta-ray foraging optimization (MRFO) algorithms. The modified chaotic MRFO algorithm improves the exploration stage and exploitation stage of the modified algorithm by employing a chaotic map in addition to weighting factors;

- The hybrid CMRFO and AEO algorithm extracts the best features of both algorithms, thus improving convergence, providing a better solution, and avoiding local minima. In addition, the use of this strategy leads to optimized and robust fractional-order control for fully bidirectional DC applications using a dual active bridge, which involves no external power flow control;
- To prove the effectiveness and robustness of the proposed FO-based PID controller, various loading disturbances were introduced to compare its performance with existing PSO-PID, AEO-PID, CMRFO-PID, and MRFO-PID controllers. Under these conditions, the newly proposed CMRFO-AEO-based fractional controller design demonstrated significant improvements in terms of performance and preserving control goals during system controllability.

The remaining sections of the paper are organized as follows: Section 2 provides the mathematical formulations of the DAB and its control. Section 3 presents the proposed fractional order-based DAB control scheme. Section 4 provides the newly proposed hybrid optimization algorithm and Section 5 presents the overall optimization process. Our results and the related discussions are provided in Section 6. The conclusions of the paper are given in Section 7.

2. Mathematical Model of Dual Active Bridge Topology

The DAB is an isolated bidirectional DC–DC converter composed of primary and secondary full bridges and interconnected through a high-frequency transformer, as shown in Figure 1. The high-frequency transformer provides galvanic isolation and energy storage through winding leakage inductance L. The transformer varies the ratio n between the primary side number of turns n_p and the secondary side number of turns n_s ($n = n_p{:}n_s$). The current flowing through the transformer does not contain a DC current component; it only contains an AC current component. In this paper, only the phase shift between the primary side and the secondary side is controlled, whereas the primary side switches are controlled with one duty cycle (u_a is applied for the switches named S_1 and its complementary signal is applied to the switches named $\overline{S_1}$). The same is applied for the secondary winding full bridge with a phase shift φ with respect to the primary side signal.

The DAB input current i_{in} to the primary side full bridge and the DAB output current i_{so} from the secondary side full bridge are, respectively, represented as:

$$i_{in} = u_a i_p \tag{1}$$

$$i_{so} = u_b i_s \tag{2}$$

where u_a and u_a are the duty cycles of the primary side bridge and secondary side bridge, respectively. In addition, i_p is the primary side transformer input current and i_s is the secondary side transformer output current of the DAB windings. The primary winding voltage v_p and secondary winding voltage v_s can be expressed in the same way, as follows:

$$v_p = u_a v_{in} \tag{3}$$

$$v_s = u_b v_o \tag{4}$$

where v_{in} represents the DC voltage input to the topology and v_o represents the DC voltage output from the topology.

Considering an ideal transformer, the relationships between voltages and currents are $\frac{v_p'}{n_p} = \frac{v_s}{n_s}$ and $n_p i_p = n_s i_s$. The primary side current i_p and the output capacitor voltage v_c are represented as state variables. Then, the DAB converter state equations can be derived as:

$$\begin{aligned} L\frac{d}{dt}i_p(t) &= v_{in}(t)u_a(t) - \frac{n_p}{n_s}v_c(t)u_b(t) \\ C\frac{d}{dt}v_c(t) &= \frac{n_p}{n_s}i_p(t)u_b(t) - i_o(t) \end{aligned} \tag{5}$$

where C is the output capacitance. The control signals $u_a(t)$ and $u_b(t)$ are defined by a sign function that has the value $-1, +1$, or 0, so periodic square-wave gate signals are given by:

$$\begin{aligned} u_a(t) &= \text{sign}(sin(\omega_s t)) \\ u_b(t) &= \text{sign}(sin(\omega_s t - \varphi)) \end{aligned} \tag{6}$$

where $\omega_s = 2\pi f_s$. The phase shift φ between signals $u_a(t)$ and $u_b(t)$ is used as the control input and is updated at every sampled time. The DAB converter can be controlled by the phase shift φ between two full bridges. For simplicity, phase-shift modulation (PSM) at the fixed switching frequency and a 0.5 duty ratio was employed, as shown in Figure 2.

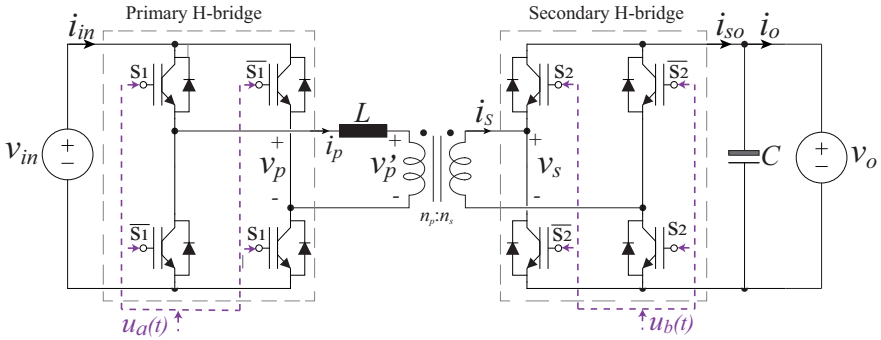

Figure 1. General scheme of the bidirectional dual active bridge converter topology.

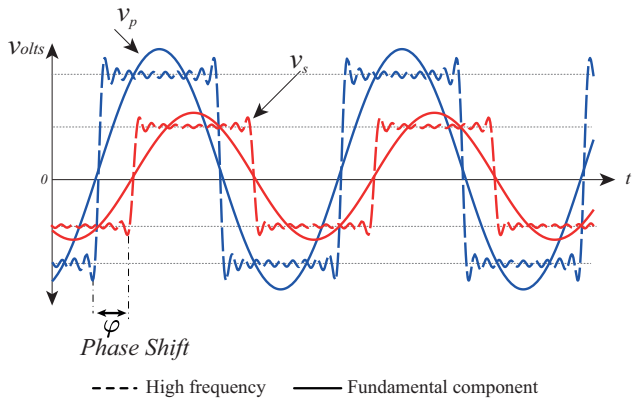

Figure 2. Illustration of the phase shift between 20°-order high-frequency switching voltages across the high-frequency transformer and also the phase shift between their corresponding fundamental components under PSM method.

2.1. Generalized Average Modelling of DAB Converter

The generalized state-space averaging (GSSA) methodology for a DAB converter was proposed in [30] and later extended in [31]. The aim of GSSA is to capture the fine details of state evolution by considering a full Fourier series. Conventional state-space averaging is a generalized average modeling method that only considers the DC term $(k = 0)$. The GSSA methodology is applied to DAB converters as follows:

$$\begin{aligned}
\langle i_p\rangle_k^{\Re} &= k\omega_s\langle i_p\rangle_k^{\Im} + \langle u_a\rangle_k^{\Re}\langle v_{in}\rangle_0 - \frac{n_p}{n_s}\langle u_b\rangle_k^{\Re}\langle v_c\rangle_0 \\
\langle i_p\rangle_k^{\Im} &= -k\omega\langle i_p\rangle_k^{\Re} + \langle u_a\rangle_k^{\Im}\langle v_{in}\rangle_0 - \frac{n_p}{n_s}\langle u_b\rangle_k^{\Im}\langle v_c\rangle_0 \\
\langle v_c\rangle_0 &= \frac{1}{C_o}\left(\frac{n_p}{n_s}\langle i_p\rangle_0\langle u_b\rangle_0 + 2\sum_{k=1}^{n}(\langle i_p\rangle_k^{\Re}\langle u_b\rangle_k^{\Re} + \langle i_p\rangle_k^{\Im}\langle u_b\rangle_k^{\Im}) - \langle i_o\rangle_0\right)
\end{aligned} \tag{7}$$

The DAB circuit's first harmonic model is developed using the GSSA. The inductor current is decomposed into two parts: one represents the active power transfer and the other the reactive power. Since it is a first harmonic approximation, higher harmonics are neglected. Hence, the fundamental component is represented by i_p $(k = -1, 1)$. Consequently, using the definition of average phasors, the zero and first indices of the control signals are obtained as follows:

$$\begin{aligned}
&\langle u_a\rangle_0 = \langle u_b\rangle_0 = 0 \\
&\langle u_a\rangle_1^{\Re} = 0; \langle u_a\rangle_1^{\Im} = -\frac{2}{\pi} \\
&\langle u_b\rangle_1^{\Re} = -\frac{2\sin\Phi}{\pi}; \langle u_b\rangle_1^{\Im} = -\frac{2\cos\Phi}{\pi}
\end{aligned} \tag{8}$$

The model consists of the three state variables. They are the $\langle v_c\rangle_0$ capacitor voltage, and two orthogonal components: imaginary $\langle i_L\rangle_1^{\Im}$ and real $\langle i_L\rangle_1^{\Re}$. The imaginary variable is in phase with the primary side AC voltage, representing the active power [32]. In the state-space model with $\dot{x} = Ax + Bu$, the state input vector is defined as:

$$x = \begin{bmatrix}\langle i_p\rangle_1^{\Re} & \langle i_p\rangle_1^{\Im} & \langle v_c\rangle_0\end{bmatrix}; u = \begin{bmatrix}\langle v_i\rangle_0 & \langle i_o\rangle_0\end{bmatrix} \tag{9}$$

2.2. Small Signal Analysis

For linear control design, the large-signal model in (7) and (9) is linearized according to the procedure presented in [30]. As shown in Table 1, the first-order derivative at the equilibrium point is used.

$$\dot{x} = \begin{bmatrix}\langle i_p\rangle_1^{\Re} & \langle i_p\rangle_1^{\Im} & \langle v_c\rangle_0\end{bmatrix} = 0 \tag{10}$$

Therefore, the small-signal transfer function representation can be calculated using the Jacobian of the system. The small-signal representation $\hat{x} = \hat{A}\hat{x} + \hat{B}\hat{d}$, where Φ is the average component of the control signal, is expressed as:

$$\hat{A} = \begin{bmatrix} 0 & \omega_s & \frac{2n\sin\Phi}{\pi L} \\ -\omega_s & 0 & \frac{2n\cos\Phi}{\pi L} \\ -\frac{4n\sin\Phi}{\pi C} & -\frac{4n\cos\Phi}{\pi C} & 0 \end{bmatrix} \tag{11}$$

$$\hat{B} = \begin{bmatrix} \frac{2n\cos\Phi}{\pi L}\langle v_c\rangle_0 \\ -\frac{2n\sin\Phi}{\pi L}\langle v_c\rangle_0 \\ -\frac{4n(\cos\Phi\langle i_p\rangle_1^{\Re} - \sin\Phi\langle i_p\rangle_1^{\Im})}{\pi C} \end{bmatrix} \tag{12}$$

Based on the state-space representation in (11) and (12), the control-to-output transfer function is defined by:

$$G(s) = (sI - \hat{A})\hat{B} \tag{13}$$

The current loop controller uses the control variable phase-shift angle φ to regulate the active power component $\langle i_L\rangle_1^{\Im}$ of the first harmonic. The parameters are listed in

Table 1 and the Bode diagram of the output current in the function of the angle is shown in Figure 3.

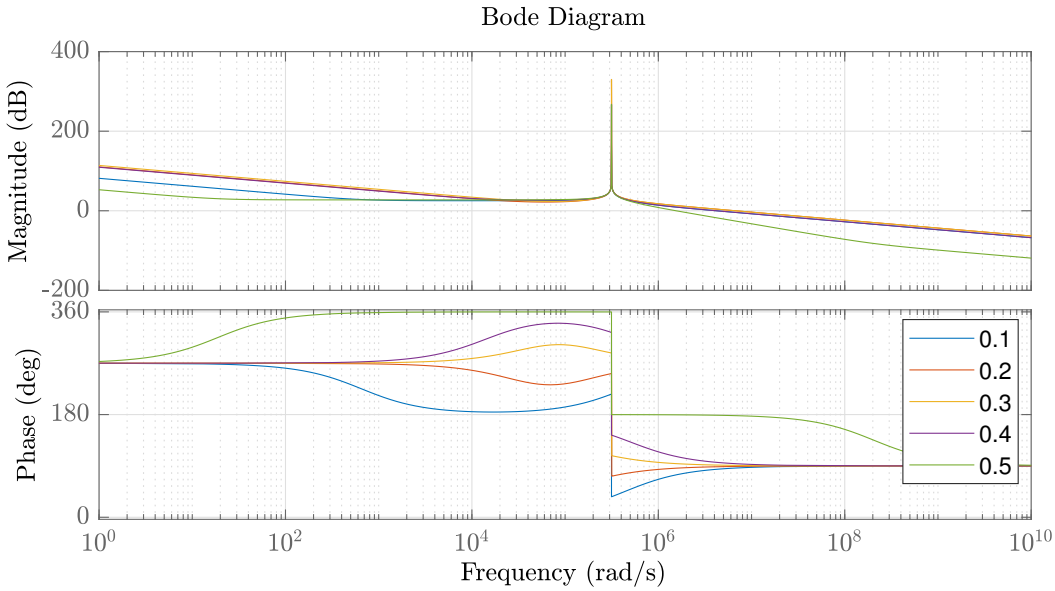

Figure 3. Bode diagram shows the influence of the percentage variation of the phase shift angle.

Table 1. System parameters for studied DAB circuit.

Parameters	Variable	Value
Input DC source nominal voltage	V_i	400 V
Output DC nominal voltage	V_o	200 V
PWM switching frequency	f_{sw}	100 KHz
Primary to secondary windings turns ratio	n (=n_p/n_s)	1.6
Power transfer inductance	L	9.8 µH
Output capacitance	C	45 µF

3. The Proposed DAB Controllers and Their Representation

3.1. Representing Fractional Controllers

A critical issue for fractional controllers is the process of their implementation to be able to implement the fractional order operators utilizing digital control kits. The general expression of fractional operators as $D^{\alpha}|_a^t$ operator can be used as [33]:

$$D^{\alpha}|_a^t = \begin{cases} \alpha > 0 \rightarrow \frac{\mathrm{d}^{\alpha}}{\mathrm{d}t^{\alpha}} & \text{FO derivative} \\ \alpha < 0 \rightarrow \int_{t_0}^{t_f} \mathrm{d}t^{\alpha} & \text{FO integral} \\ \alpha = 0 \rightarrow 1 \end{cases} \tag{14}$$

$$D^{\alpha}|_a^t = \lim_{h \to 0} \frac{1}{h^{\alpha}} \sum_{r=0}^{\frac{t-a}{h}} (-1)^r \binom{n}{r} f(t - rh) \tag{15}$$

where h is the stepping time and $[\cdot]$ refers to integer-based terms for the operator representation in the Grunwald–Letnikov-based definition. In (15), the range for n is $(n-1 < \alpha < n)$, with binomial coefficients being expressed as follows [34]:

$$\binom{n}{r} = \frac{\Gamma(n+1)}{\Gamma(r+1)\Gamma(n-r+1)'} \tag{16}$$

where gamma in (16) represents a function determined by [33]:

$$\Gamma(n+1) = \int_0^\infty t^{x-1} e^{-t}\, dt \tag{17}$$

In the Riemann–Liouville-based definition, the sum and limits are avoided using integer derivatives/integrals as follows [35]:

$$D^\alpha|_a^t = \frac{1}{\Gamma(n-\alpha)} \left(\frac{d}{dt}\right)^n \int_a^t \frac{f(\tau)}{(t-\tau)^{\alpha-n+1}}\, d\tau \tag{18}$$

In the Caputo-based definition, the fractional operator is determined as follows [34]:

$$D^\alpha|_a^t = \frac{1}{\Gamma(n-\alpha)} \int_a^t \frac{f^{(n)}(\tau)}{(t-\tau)^{\alpha-n+1}}\, d\tau \tag{19}$$

A more convenient way for digital processors to implement fractional operators is through Oustaloup recursive approximation (ORA). ORA has been shown to be more easily implementable than other methods, especially for digital signal processors (DSPs) [33]. Therefore, ORA was utilized within this study for fractional operators and the developed control methods. The αth-based operators (s^α) for ORA derivatives were mathematically determined using [33]:

$$s^\alpha \approx \omega_h^\alpha \prod_{k=-N}^{N} \frac{s+\omega_k^z}{s+\omega_k^p} \tag{20}$$

where $\omega_{\mathrm{k}}^{\mathrm{p}}$ and $\omega_{\mathrm{k}}^{\mathrm{z}}$ are representations of the poles' and zeros' locations, respectively, for the ω_h sequence. Their related calculations are as follows:

$$\omega_k^z = \omega_b \left(\frac{\omega_h}{\omega_b}\right)^{\frac{k+N+\frac{1-\alpha}{2}}{2N+1}} \tag{21}$$

$$\omega_k^p = \omega_b \left(\frac{\omega_h}{\omega_b}\right)^{\frac{k+N+\frac{1+\alpha}{2}}{2N+1}} \tag{22}$$

$$\omega_h^\alpha = \left(\frac{\omega_h}{\omega_b}\right)^{\frac{-\alpha}{2}} \prod_{k=-N}^{N} \frac{\omega_k^p}{\omega_k^z} \tag{23}$$

There are $(2N+1)$ poles/zeros in an ORA scheme of N order. Within this paper, the ORA representation for the fifth order $(N = 5)$ and $(\omega \in [\omega_{\mathrm{b}}, \omega_{\mathrm{h}}])$ is equal to $[10^{-3}, 10^{3}]$ rad/s range of frequency. The selection of $N = 5$ was made by analyzing the frequency response at different values of N. Compared to the ORA representation at $N = 3$, the ORA representations at $N = 5$ and $N = 7$ provide better representations. The resulting transfer function based on the poles/zeros number derived from $(2N+1)$ leads to having an order of 7 at $N = 3$, 11 at $N = 5$, and 15 at $N = 7$. Accordingly, the ORA representation with $N = 5$ was selected in this study as it gives a near-precise representation with a reduced-order transfer function.

3.2. The Proposed DAB Based Fractional Controllers

The FO control mechanism gives an additional degree of freedom in system control and is used as a feedback control tool. The transfer functions for both integer-order and FO control systems are expressed as follows:

$$
\begin{aligned}
PI(s) &= k_p + \frac{k_i}{s} \\
PID(s) &= k_p + \frac{k_i}{s} + k_d s \\
FOPI(s) &= k_p + \frac{k_i}{s^\lambda} \\
FOPID(s) &= k_p + \frac{k_i}{s^\lambda} + k_d s^\mu
\end{aligned}
\tag{24}
$$

Proper determination of the controller parameters k_p, k_i, μ, and λ, can improve the performance of DAB during transients and steady-state conditions. The optimization process tunes these parameters simultaneously to determine the optimized parameters based on the objective function. Figure 4 shows the block diagram of the controller. This work uses the widely-used error estimation methods used in the proposed optimization process, due to their low computational cost. The considered methods are the integral-squared error (ISE), and the integral absolute error (IAE). The methods are used to verify the effectiveness and superiority of the proposed controller and optimizer based on the desired limitations and specifications. They are represented as follows:

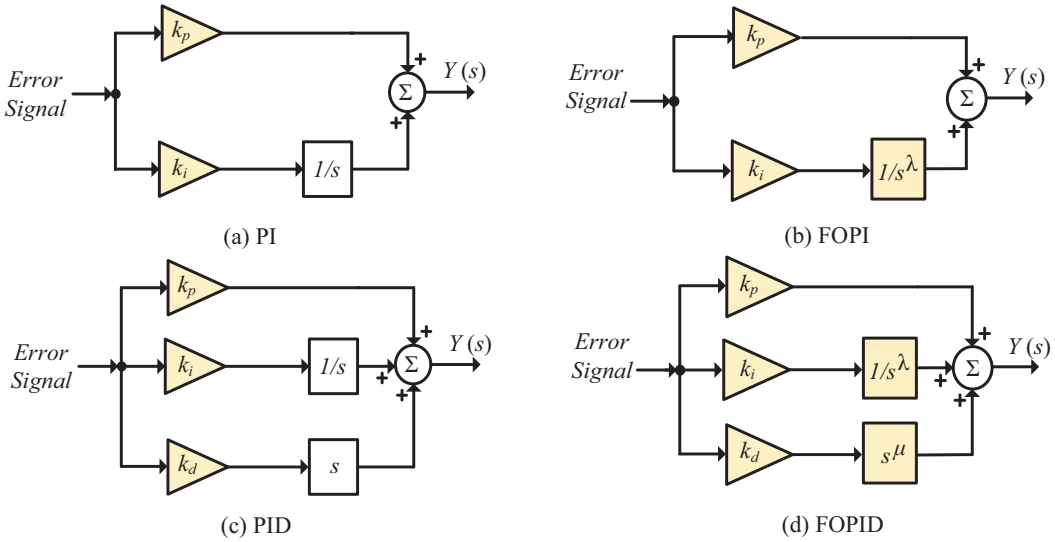

Figure 4. Block diagram of the integer order and the fractional order.

The proper determination of the controller parameters k_p, k_i, μ, and λ can improve the performance of the DAB during transient and steady-state conditions. The optimization process simultaneously optimizes these parameters based on the objective function. Figure 4 shows the block diagram of the controller. In this study, we selected the widely used integral-squared error (ISE) and integral absolute error (IAE) estimation methods for the optimization process due to their low computational cost. The methods were used to verify the effectiveness and superiority of the proposed controller and optimizer based on certain limitations and specifications. They are represented as follows:

$$
\begin{aligned}
ISE &= \int_a^b e^2 \, dx \\
IAE &= \int_a^b abs(e) \, dx
\end{aligned}
\tag{25}
$$

To date, there is no straightforward method for determining optimal FO controller parameters using traditional techniques. Generally, metaheuristic optimization algorithms are employed to find the optimal parameter values to improve their performance.

4. Proposed Hybrid Optimization Method

The artificial ecosystem-based optimization (AEO) algorithm is one of the most recent metaheuristic algorithms and was inspired by the energy flow in a natural ecosystem [36]. The results in [37] demonstrate that the AEO algorithm outperforms other optimization methods in terms of convergence rate. Nonetheless, it can fall into local minima due to its fast convergence rate. Another representative and novel metaheuristic method is the manta-ray foraging optimization (MRFO) algorithm, which simulates the foraging strategy and behavior of manta-ray groups [38]. The MRFO algorithm exhibits robust global search capabilities and high stability, making it a reliable choice for complex optimization tasks. Recently, a popular approach is that of metaheuristic algorithm hybridization, which attempts to combine the desirable properties of different algorithms to mitigate their individual weaknesses.

4.1. Conventional AEO Algorithm

The AEO algorithm is based on the energy flow in a natural ecosystem [39]. This optimization method is divided into three main steps: production, consumption, and decomposition.

- *Production*: In this step, the main goal is to enhance the balance between exploitation and exploration processes. This phase can be modeled using the following mathematical expressions:

$$x_1(t-1) = (1-a)x_n(t) + ax_{rand}(t) \tag{26}$$

$$a = (1 - \frac{t}{max_iter})r_1 \tag{27}$$

$$x_{rand} = r(U_b - L_b) + L_b \tag{28}$$

  where t depicts the current iteration, n is the population size, a is a linear weight coefficient, x_{rand} is a random position, max_iter represents the total number of iterations, r_1 is a random number in the range of [0,1], L_b is the lower bound, and U_b is the upper bound;
- *Consumption*: Based on the feature of Levy flight feature, the following consumption factor is used:

$$C = \frac{1}{2}\frac{v_1}{|v_2|} \tag{29}$$

$$v_1 \sim N(0,1), v_2 \sim N(0,1) \tag{30}$$

  where $N(0,1)$ is a normal distribution with a mean = 0 and standard deviation = 1. Furthermore, three types of consumers can be randomly selected, and each consumer adopts different consumption strategies.
  Herbivore is represented with the following expression:

$$x_i(t+1) = x_i(t) + C \cdot (x_i(t) - x_1(t)), i \in [2, \ldots, n] \tag{31}$$

  Carnivore is mathematically formulated as follows:

$$\begin{cases} x_i(t+1) = x_i(t) + C \cdot (x_i(t) - x_j(t)), \\ i \in [2, \ldots, n] \\ j = randi([2i-1]) \end{cases} \tag{32}$$

  Omnivore can be modeled as

$$\begin{cases} x_i(t+1) = x_i(t) + C \cdot (x_i(t) - x_1(t)) + (1-r_2), \\ (x_i(t) - x_j(t)), i = 3, \cdots, n \\ j = randi([2i-1]) \end{cases} \tag{33}$$

- *Decomposition*: In this step, a decomposition factor D, and the weight coefficients e and h are introduced. Depending on the aforementioned parameters and the decomposer x_n, the i-th individual position x_i can be enhanced to a better position. The equations that describe this process are described as follows:

$$x_i(t+1) = x_n(t) + D \cdot (e \cdot x_n(t) - h \cdot x_i(t)), i = 1, \ldots, n \tag{34}$$

$$D = 3u, u \sim N(0,1) \tag{35}$$

$$e = r_3 \cdot randi([12]) - 1 \tag{36}$$

$$h = 2 \cdot r_3 - 1 \tag{37}$$

4.2. Conventional CMRFO Algorithm

The chaotic MRFO algorithm is one of the latest metaheuristic algorithms. It simulates the foraging behaviors of manta rays [36]. CMRFO differs from most metaheuristic algorithms in that, instead of being a random-based optimization technique, it benefits from the superior statistical and dynamical properties of logistic chaos maps [40]. The mathematical behavior of the CMRFO algorithm can be described as follows:

- *Chain foraging and cyclone foraging*

$$x_i(t+1) = \begin{cases} x_i(t) + r_1 \cdot (x_{best}(t) - x_i(t)) + \gamma \cdot (x_{best}(t) - x_i(t)), i = 1 \\ x_i(t) + r_2 \cdot (x_{i-1}(t) - x_i(t)) + \gamma \cdot (x_{best}(t) - x_i(t)), i = 2, \cdots, n \end{cases} \tag{38}$$

where r_1 and r_2 are random numbers, x_i is the position of the i-th individual, and x_{best} is a high concentration of plankton. In addition, $\gamma = 2 \cdot r_1 \sqrt{|log(r_1)|}$ when chain foraging occurs. On the other hand, for cyclone foraging, $\gamma = 2e^{r_2 \cdot \frac{max_{iter} - t + 1}{max_{iter}}} \cdot sin(2\pi r_2)$. The equation used to generate a new position for each individual in the search space is as follows:

$$x_{rand} = L_b + r \cdot (U_b - L_b) \tag{39}$$

$$x_i(t+1) = \begin{cases} x_{rand} + r_1 \cdot (x_{rand} - x_i(t)) + \gamma \cdot (x_{rand} - x_i(t)), i = 1 \\ x_{rand} + r_2 \cdot (x_{i-1}(t) - x_i(t)) + \gamma \cdot (x_{rand} - x_i(t)), i = 2, \cdots, n \end{cases} \tag{40}$$

where x_{rand} is the position produced to replace r in (39) with the following chaotic array:

$$z_{k+1} = 4z_k(1 - z_k) \tag{41}$$

- *Somersault foraging*: The mathematical model of somersault is given by:

$$x_i(t+1) = x_i(t) + 2(r_3 \cdot x_{best} - r_4 \cdot x_i(t)) \tag{42}$$

where r_3 and r_4 are random numbers in the range [0,1].

4.3. Hybrid AEO-CMRFO

Considering the best solution given by the AEO algorithm to be $x_{AEO}(t)$ and the best solution given by the CMRFO to be $x_{CMRFO}(t)$ at time t, the hybrid combination is performed as follows:

$$x_{hybrid}(t) = \lambda(t) \cdot x_{AEO}(t) - [1 - \lambda(t)] \cdot x_{CMRFO}(t) \tag{43}$$

where $\lambda(t)$ is a function in the range $[0, 1]$. This function is used to select the metaheuristic algorithm as a function of time at each iteration and it is defined by [41]:

$$\lambda(t) = \frac{1}{1 + e^{-a(t)}} \tag{44}$$

where $a(t)$ is an auxiliary parameter used to minimize the instantaneous square error of the controllers, which is obtained as follows:

$$a(t+1) = a(t) + \mu_a \cdot e(1) \cdot \{e_{AEO}(t) - e_{CMRFO}(t)\} \cdot \lambda(t) \cdot [1 - \lambda(t)] \quad (45)$$

5. Proposed Hybrid AEO-CMRFO Methodology for Controller Tuning

The methodology involved selecting candidate algorithms to generate the hybrid algorithm. The selected algorithms were those with the fastest convergence and highest accuracy. Optimization was primarily evaluated using the performance indicators ISE and IAE. The system for evaluating performance was the DAB topology, which was configured to operate with a constant frequency phase-shift modulation. The full-bridge circuits can generate a square-wave AC voltage at their terminals. The primary side bridge did not require any delay and operated at a constant duty cycle of 50% and a constant frequency of 10 kHz. The phase-shift angle was controlled by the secondary side bridge, which generated a delayed square wave with a 50% duty cycle. This approach maintained a constant duty cycle, thus reducing the control complexity.

Finally, the algorithms were evaluated and compared to the hybrid algorithm. Subsequently, after hybrid algorithm validation, the controller parameters were tuned. The performance of different PI, FOPI, and FOPID controllers was then compared. The selection results are presented in Figures 5 and 6. Moreover, the obtained statistical analysis results of IAE and ISE are shown in Table 2 and Table 3, respectively.

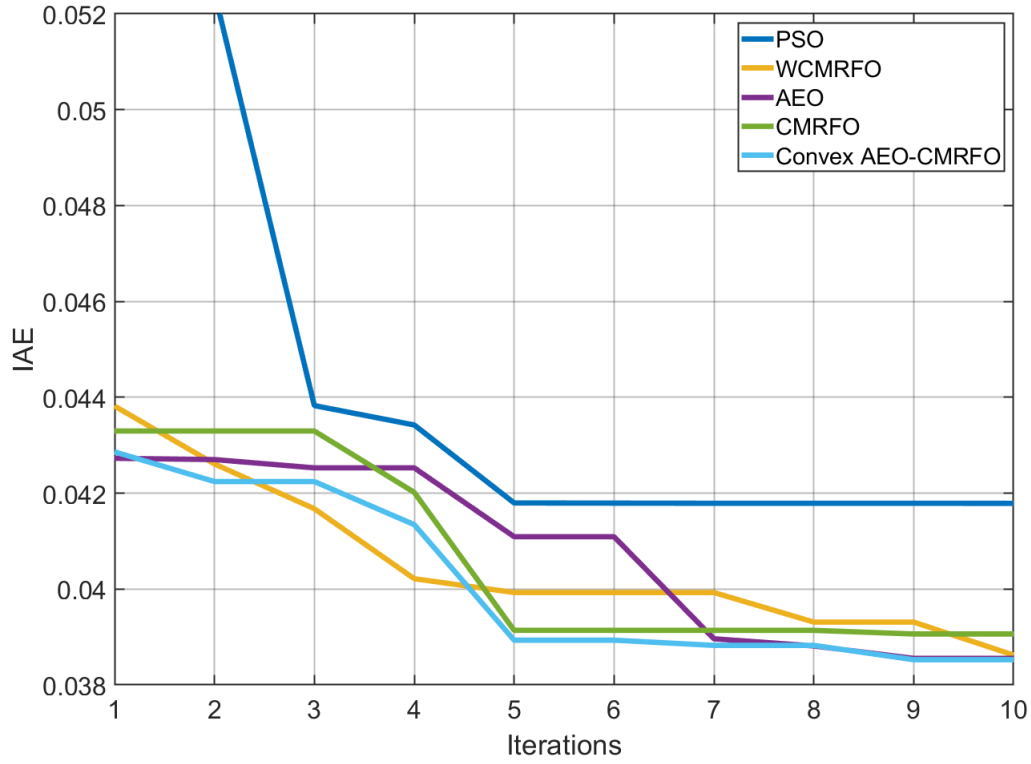

Figure 5. Graph of simulation results for IAE-based comparison of proposed hybrid AEO-CMRFO algorithm and other approaches.

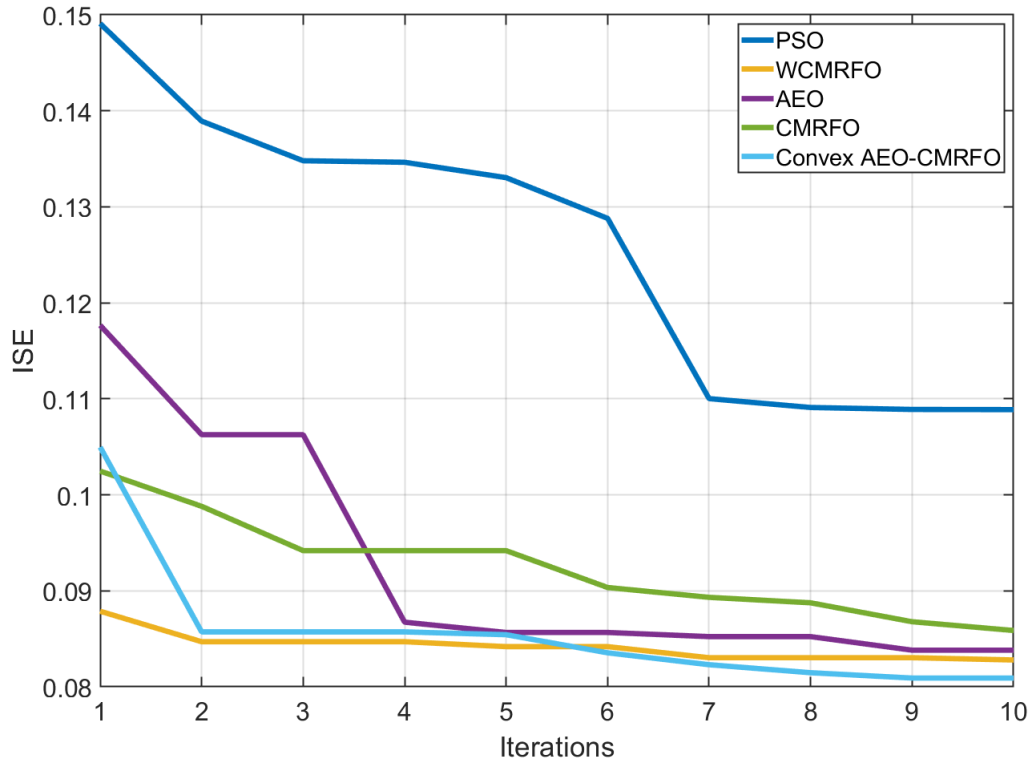

Figure 6. Graph of simulation results for ISE-based comparison of proposed hybrid AEO-CMRFO algorithm and other approaches.

Table 2. Results of IAE-based comparison of proposed hybrid AEO-CMRFO algorithm and other approaches.

	IAE		
	Standard Deviation	**Best Value**	**Median Value**
PSO	0.0043	0.0417	0.0442
AEO	0.0019	0.0386	0.0408
CMRFO	0.0020	0.0391	0.0407
WCMRFO	0.0016	0.0386	0.0405
Proposed hybrid AEO-CMRFO	0.0018	0.0385	0.0401

Table 3. Results of ISE-based comparison of proposed hybrid AEO-CMRFO algorithm and other approaches.

	ISE		
	Standard Deviation	**Best Value**	**Median Value**
PSO	0.0150	0.1089	0.1256
AEO	0.0125	0.0838	0.0926
CMRFO	0.0053	0.0859	0.0925
WCMRFO	0.0015	0.0828	0.0842
Proposed hybrid AEO-CMRFO	0.0022	0.0807	0.0835

Controllers Optimization Process

It is crucial to determine a set of optimum parameter values for the FO controller using the correct objective function to improve the system dynamics. Error minimization

function-based current control was selected and implemented in the objective cost function formulation of the bidirectional DAB current control optimization problem in this study. Figure 7 shows a schematic process representation of FO control optimization using the hybrid algorithm. The process is described as follows:

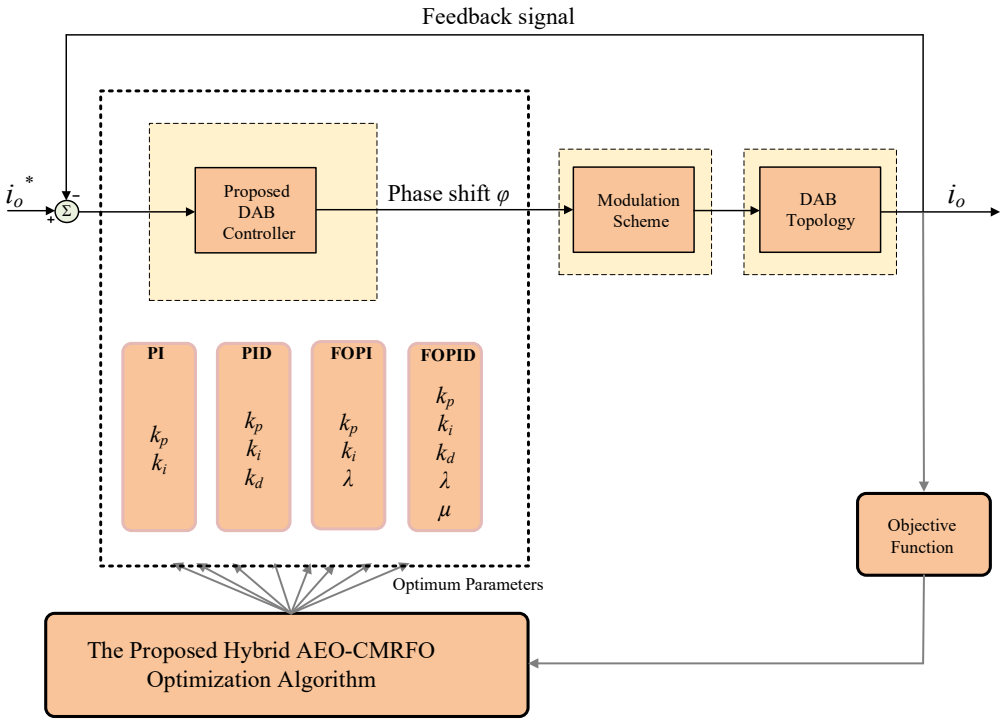

Figure 7. Overall proposed DAB controller process using proposed hybrid AEO-CMRFO algorithm.

- The DAB and its control structure are implemented. The measured current error is used to construct the fitness function of the proposed design method. In this study, the ISE and IAE error functions were formulated as driving fitness functions. The calculated fitness function is fed into the proposed hybrid algorithm to optimally determine the FO control parameters.
- Then, the initial parameter set of each individual is generated using the hybrid algorithm. The set is determined by controller type and the possible parameters to tune (for example, K_p, K_i, K_d, λ, and μ in this paper). The boundary limits for each tunable parameter are determined through pre-designed controllers using conventional design schemes from the literature to guarantee the stability and convergence characteristics of the designed controllers. Table 4 shows the threshold values for tuning K_p, K_i, K_d, λ, and μ;

Table 4. Minimum and maximum values used to tune K_p, K_i, K_d, λ and μ.

Threshold	K_p	K_i	λ	K_d	μ
Minimum	0	0	0.1	0	0.1
Maximum	6.0	500	0.3	1.0	0.5

- The item algorithm encoded the parameter solution set using binary codes (named strings). The design fitness function is evaluated each time via an iterating scheme based on a given set of individuals, as in Step 2;
- Afterward, the proposed algorithm selects the most suitable members among the populations based on the resulting fitness function of each set. The weakest members are excluded from the solution. Hence, this theory follows natural selection and logic

theory. After reaching the iteration number, the parameter set providing the best global value is used to determine the optimum values. In this case, the fitness value does not increase with the iteration number;

- At this point, the desired optimum solution is utilized by the implemented FO control method, which utilizes the DAB controller as an optimized feedback system.

A schematic diagram of the proposed DAB controllers' optimization process using the newly proposed hybrid AEO-CMRFO is shown in Figure 7. The modeled DAB along with its modulation system, which generates the pulses required to drive the semiconductor switches, was produced using Matlab Simulink. The modeled system was linked with an m-file in Matlab, which contained the optimization algorithm and the parameter and algorithm setting search boundaries. The proposed hybrid AEO-CMRFO algorithm was responsible for searching for and determining the best parameter set from the optimization range to optimize the predefined objective function. The proposed hybrid AEO-CMRFO algorithm was run, and during each iteration, an objective function calculation was performed and the result was compared with the previously stored global optimum objective function value. Then, in the case of having a lower objective function value in the current iteration compared to the previously stored optimum value, the objective function value was updated. After reaching the maximum number of iterations and the stop criteria, the optimum parameter set was output as the associated convergence curves of evaluated algorithms. These values represented the best set, and they were used to simulate the DAB system.

6. Simulation Results

In this section, we evaluate the dynamical response results of the optimized controllers using the hybrid algorithm. The analysis is divided into two parts: a comparison of the results of the different controllers, i.e., PI, FOPI, and FOPID, and the analysis of the performance indicators and optimization function. The simulations in this section were carried out using Matlab as the development environment. In addition, the m-file contained the implemented hybrid combination CMRFO-AEO optimization program. This m-file was used to tune all the parameters of the PI, FOPI, and FOPID controllers. These parameters included $k_p, k_i, k_d, \mu, \lambda$, which were obtained for the objective function for the bidirectional power flow control of the DAB. This Matlab file was linked to the Simulink model of the DAB to carry out the optimization process, which involved eight populations and a maximum number of iterations of 100. The optimal solution of the optimization process was established after performing 10 separate runs, which corresponded to minimum ISE and IAE values that were captured and used as the final controller parameters.

6.1. Controllers Response

Step Response: When a step input was made, the system response achieved at the end of the hybrid algorithm is given in Figure 8. For the regulatory response with a disturbance at t = 0.02 s, a perturbation from $I_o = 10A$ to $I_o = -10A$ steps was introduced at the output end of the system. The following response represents the performance in terms of bidirectional power control and the regulatory response parameter specifications. The optimal values of PI using different algorithms are shown in Table 5.

Figure 8 shows the control response of the DAB converter controlled by PI, FOPI, and FOPID. The control system was stable and robust, as shown in the graph. The results confirm that the FOPID and PI controllers, which were used to ensure that the dual active bridge converter closed loop was stable, were able to produce the desired results in terms of control response. The ripple of the output current was 6%. Moreover, it was observed that the output current followed the setpoint even when the current changed bidirectionally.

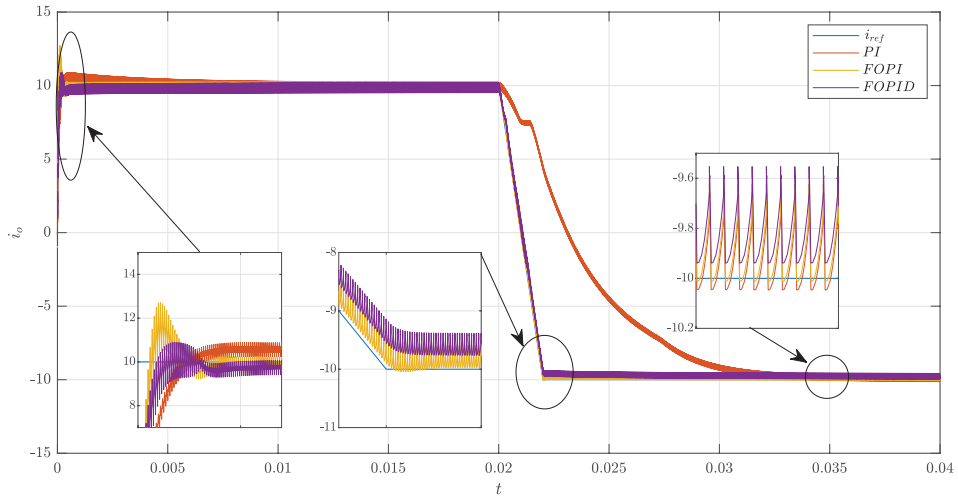

(**a**) ISE

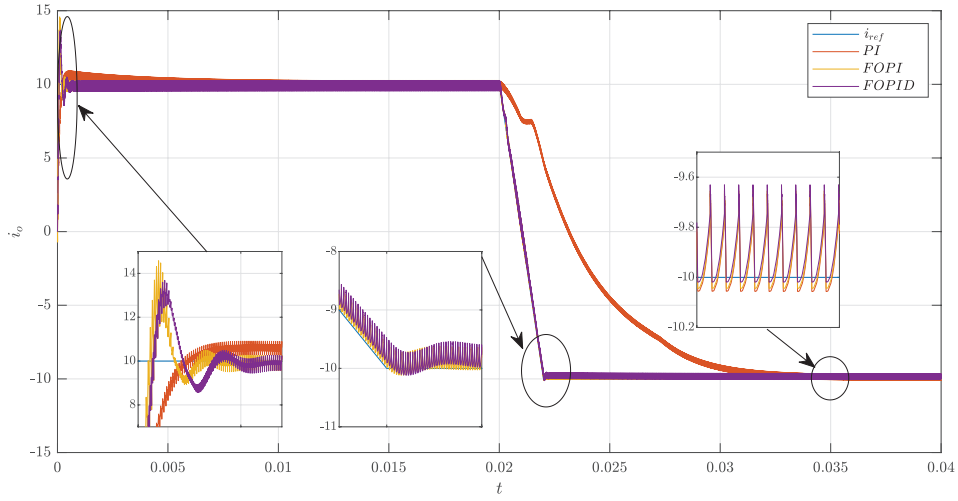

(**b**) IAE

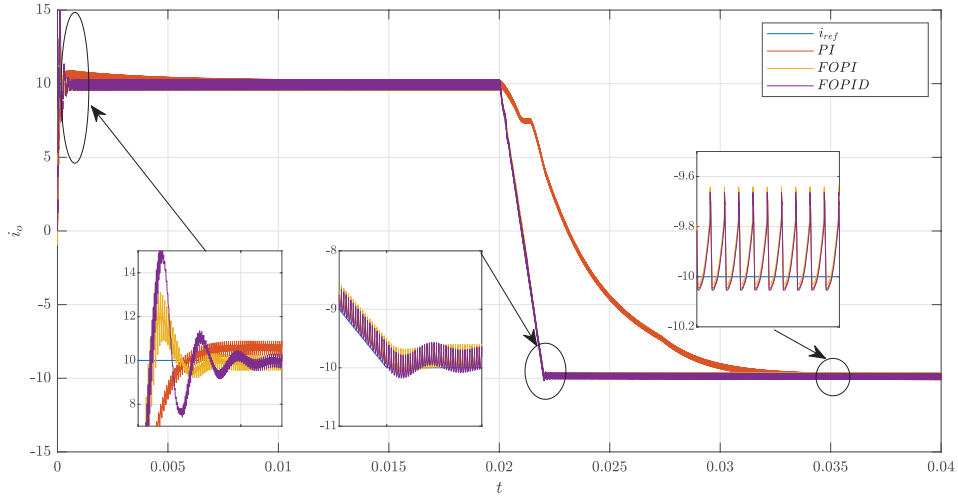

(**c**) ISE + IAE

Figure 8. Comparison of the current controller time response.

Table 5. Results of best iteration value of controller parameters.

	ISE			IAE			ISE + IAE		
	PI	**FOPI**	**FOPID**	**PI**	**FOPI**	**FOPID**	**PI**	**FOPI**	**FOPID**
k_p	0.5	5.4	5.56	0.44	1.62	1.75	0.49	3.52	0.34
k_i	750	366	394.5	745	283.4	454.4	748	330.2	353
λ	-	0.19	0.29	-	0.12	0.15	-	0.107	0.10
k_d	-	-	0.13	-	-	0.102	-	-	0.35
μ	-	-	0.322	-	-	0.182	-	-	0.978

6.2. Cost Function

Different performance indices were calculated for the studied controllers, as tabulated in Table 6. The comparison included ISE and IAE values for the different controllers. Table 6 shows that the proposed controller achieved improved values for all of the calculated performance indices in various system scenarios. Moreover, the evaluated performance indices illustrate the superiority of the proposed controller over the traditional controllers. For example, in PI case 1, the ISE value was 0.4828 and the IAE value was 0.0618, and for the proposed FOPI and FOPID designs, the ISE value was 0.0052 and the IAE value was 0.00080721. It can be also observed that the ISE values using the proposed control method were 15.52% and 23.74% lower than the ISE values using the PI and FO controllers, respectively. Furthermore, the IAE values were 0.2665, 0.1941, and 0.1022 for the PI, FOPI, and proposed control, respectively. In addition, the IAE values for the proposed control were 38.35% and 52.65% lower than the IAE values of the PI and FO controllers, respectively. In summary, the proposed controller produced superior performance indices compared to the other controllers. These performance indices demonstrate the superiority of the proposed controller in all the studied scenarios using various performance objectives.

Table 6. Average cost function convergence for proposed hybrid AEO-CMRFO method.

Controller	**ISE**	**IAE**	**ISE + IAE**
PI	0.4828	0.0618	0.5281
FOPI	0.0031	0.0063	0.0093
FOPID	0.0031	0.0055	0.0085

6.3. Discussion

The targeted application of the proposed control design and hybrid optimization algorithm is the bidirectional power transfer using the DAB topology. Therefore, a step change in the reference current in both directions is important to evaluate the proposed design and control response. The evaluation criteria included the overshot, response time, and steady-state ripple values. The proposed FOPID outperformed the other proposed controllers. The proposed FOPI design came in second from a performance metrics point of view. Additionally, ISE and IAE values were evaluated for the studied controllers. The IAE values for the proposed control were 38.35% and 52.65% lower than the IAE values with the PI and FO controllers, respectively. In summary, the proposed controller produced the best performance indices compared to the other addressed controllers. These performance indices demonstrate the superiority of the proposed controller in all the studied scenarios using various performance objectives.

7. Conclusions

In this paper, a hybrid combination of two metaheuristic algorithms—AEO and CM-RFO—is proposed for the first time, with the intention of improving the robustness of

fractional-order PID controllers for DAB-based applications. The DAB is capable of providing high performance in a wide range of applications. However, this cannot be achieved if the DAB only uses conventional integer-order PID controllers. In particular, the proposed hybrid AEO-CMRFO algorithm exploits the high convergence rate of the AEO algorithm and the robust global search capabilities of the CMRFO algorithm. Therefore, the proposed method achieves a higher convergence speed and lower steady-state error by combining the two optimizers in parallel. In addition, it outperformed all of the compared algorithms in terms of the best and mean values. It was, therefore, shown that using hybrid combinations of stochastic optimization methods can significantly improve the performance of FOPI and FOPID controllers. When the FO controller parameters were optimally selected, the entire control system exhibited better dynamic and steady-state performance compared to traditional PI controllers. The proposed hybrid algorithm demonstrated its ability to robustly tune FO control to overcome the bidirectional power of the system by reducing overshoot and settling times. In addition, the integral squared errors formed the final objective function ISE, which was the best optimization cost function. The obtained values were the average of the minimum compared to the IAE and the combined ISE-IAE. Based on the results, the fractional-order PID controllers produced superior results when compared with the conventional PI controllers. Consequently, this led to an improvement in bidirectional power flow control in the DAB systems. Future research will focus on improving the implementation and efficiency of DAB converters.

Author Contributions: Conceptualization, E.P. and F.R.; Data curation, F.R. and E.P.; Formal analysis, G.S.; Investigation, E.V. and J.G.A.; Methodology, J.G.A. and G.S.; Resources, E.P., M.A. and E.V.; Software, M.A., E.P. and F.R.; Supervision, G.S. and J.G.A.; Validation, E.P. and F.R.; Writing—original draft, M.A. and G.S.; Writing—review and editing, G.S. and M.A. All authors have read and agreed to the published version of the manuscript.

Funding: The authors would like to thank the Instituto Politécnico Nacional for the financial support. This research was also funded by Agencia Nacional de Investigacion y Desarrollo (ANID) Chile, FONDECYT Iniciación 11230430, VIU23PO127 and SERC-Chile ANID/FONDAP/1523A0006.

Data Availability Statement: Data are contained within the article.

Acknowledgments: The authors would like to thank the Consejo Nacional de Humanidades, Ciencias y Tecnologías (CONAHCYT) and the Instituto Politécnico Nacional for the financial support. This research was also funded by Agencia Nacional de Investigación y Desarrollo (ANID) Chile, FONDECYT Iniciación 11230430, VIU23PO127 and SERC-Chile ANID/FONDAP/1523A0006.

Conflicts of Interest: The authors declare no conflicts of interest.

References

1. IPCC. *2023: Climate Change 2023: Synthesis Report. Contribution of Working Groups I, II and III to the Sixth Assessment Report of the Intergovernmental Panel on Climate Change*; Core Writing Team, Lee, H., Romero, J., Eds.; IPCC: Geneva, Switzerland, 2023. [CrossRef]
2. Rodriguez, J.; Blaabjerg, F.; Kazmierkowski, M.P. Energy Transition Technology: The Role of Power Electronics. *Proc. IEEE* **2023**, *111*, 329–334. [CrossRef]
3. Xu, Q.; Vafamand, N.; Chen, L.; Dragičević, T.; Xie, L.; Blaabjerg, F. Review on Advanced Control Technologies for Bidirectional DC/DC Converters in DC Microgrids. *IEEE J. Emerg. Sel. Top. Power Electron.* **2021**, *9*, 1205–1221. [CrossRef]
4. He, P.; Khaligh, A. Comprehensive Analyses and Comparison of 1 kW Isolated DC–DC Converters for Bidirectional EV Charging Systems. *IEEE Trans. Transp. Electrif.* **2017**, *3*, 147–156. [CrossRef]
5. Stynski, S.; Luo, W.; Chub, A.; Franquelo, L.G.; Malinowski, M.; Vinnikov, D. Utility-Scale Energy Storage Systems: Converters and Control. *IEEE Ind. Electron. Mag.* **2020**, *14*, 32–52. [CrossRef]
6. Ruiz, F.; Perez, M.A.; Espinosa, J.R.; Gajowik, T.; Stynski, S.; Malinowski, M. Surveying Solid-State Transformer Structures and Controls: Providing Highly Efficient and Controllable Power Flow in Distribution Grids. *IEEE Ind. Electron. Mag.* **2020**, *14*, 56–70. [CrossRef]
7. Tong, A.; Hang, L.; Li, G.; Jiang, X.; Gao, S. Modeling and Analysis of a Dual-Active-Bridge-Isolated Bidirectional DC/DC Converter to Minimize RMS Current With Whole Operating Range. *IEEE Trans. Power Electron.* **2018**, *33*, 5302–5316. [CrossRef]
8. Shao, S.; Chen, H.; Wu, X.; Zhang, J.; Sheng, K. Circulating Current and ZVS-on of a Dual Active Bridge DC-DC Converter: A Review. *IEEE Access* **2019**, *7*, 50561–50572. [CrossRef]

9. Krismer, F.; Kolar, J.W. Efficiency-Optimized High-Current Dual Active Bridge Converter for Automotive Applications. *IEEE Trans. Ind. Electron.* **2012**, *59*, 2745–2760. [CrossRef]
10. Segaran, D.; Holmes, D.G.; McGrath, B.P. Enhanced Load Step Response for a Bidirectional DC–DC Converter. *IEEE Trans. Power Electron.* **2013**, *28*, 371–379. [CrossRef]
11. Veeramraju, K.J.P.; Kimball, J.W. Dynamic Model of AC–AC Dual Active Bridge Converter Using the Extended Generalized Average Modeling Framework. *IEEE Trans. Power Electron.* **2024**, *39*, 3558–3567. [CrossRef]
12. Rim, C.; Cho, G. Phasor transformation and its application to the DC/AC analyses of frequency phase-controlled series resonant converters (SRC). *IEEE Trans. Power Electron.* **1990**, *5*, 201–211. [CrossRef]
13. Scandola, L.; Corradini, L.; Spiazzi, G. Small-Signal Modeling of Uniformly Sampled Phase-Shift Modulators. *IEEE Trans. Power Electron.* **2015**, *30*, 5870–5880. [CrossRef]
14. Arena, G.; Vinnikov, D.; Chub, A.; De Carne, G. Accuracy Analysis of Dual Active Bridge Simulations under Different Integration Methods. In Proceedings of the 2022 AEIT International Annual Conference (AEIT), Rome, Italy, 3–5 October 2022; pp. 1–6. [CrossRef]
15. Rolak, M.; Twardy, M.; Soból, C. Generalized Average Modeling of a Dual Active Bridge DC-DC Converter with Triple-Phase-Shift Modulation. *Energies* **2022**, *15*, 6092. [CrossRef]
16. Dòria-Cerezo, A.; Serra, F.M.; Esteban, F.D.; Biel, D.; Griñó, R. Comparison of First- and Second-Order Sliding-Mode Controllers for a DC-DC Dual Active Bridge. *IEEE Access* **2022**, *10*, 40264–40272. [CrossRef]
17. Podlubny, I. Fractional-order systems and PI/sup /spl lambda//D/sup /spl mu//-controllers. *IEEE Trans. Autom. Control* **1999**, *44*, 208–214. [CrossRef]
18. Travieso-Torres, J.C.; Contreras-Jara, C.; Diaz, M.; Aguila-Camacho, N.; Duarte-Mermoud, M.A. New Adaptive Starting Scalar Control Scheme for Induction Motor Variable Speed Drives. *IEEE Trans. Energy Convers.* **2022**, *37*, 729–736. [CrossRef]
19. Aguila-Camacho, N.; García-Bustos, J.E.; Castillo-López, E.I.; Gallegos, J.A.; Travieso-Torres, J.C. Switched Fractional Order Model Reference Adaptive Control for First Order Plants: A Simulation-Based Study. *J. Dyn. Syst. Meas. Control* **2022**, *144*, 044502. [CrossRef]
20. Aguila-Camacho, N.; Duarte-mermoud, M.A. Improving the control energy in model reference adaptive controllers using fractional adaptive laws. *IEEE/CAA J. Autom. Sin.* **2016**, *3*, 332–337. [CrossRef]
21. Bošković, M.Č.; Šekara, T.B.; Stojić, D.M.; Rapaić, M.R. Novel tuning rules for PIDC controllers in automatic voltage regulation systems under constraints on robustness and sensitivity to measurement noise. *Int. J. Electr. Power Energy Syst.* **2024**, *157*, 109791. [CrossRef]
22. Petras, I. The fractional-order controllers: Methods for their synthesis and application. *arXiv* **2000**, arXiv:math.OC/math/0004064.
23. Vinagre, B.; Podlubny, I.; Dorcak, L.; Feliu, V. On Fractional PID Controllers: A Frequency Domain Approach. *IFAC Proc. Vol.* **2000**, *33*, 51–56. [CrossRef]
24. Luo, Y.; Chen, Y. Stabilizing and robust fractional order PI controller synthesis for first order plus time delay systems. *Automatica* **2012**, *48*, 2159–2167. [CrossRef]
25. Dorcak, L.; Petras, I.; Kostial, I.; Terpak, J. State-Space Controller Design for the Fractional-Order Regulated System. *arXiv* **2002**, arXiv:math.OC/math/0204189.
26. Merrikh-Bayat, F. A uniform LMI formulation for tuning PID, multi-term fractional-order PID, and Tilt-Integral-Derivative (TID) for integer and fractional-order processes. *ISA Trans.* **2017**, *68*, 99–108. [CrossRef] [PubMed]
27. Nassef, A.M.; Abdelkareem, M.A.; Maghrabie, H.M.; Baroutaji, A. Metaheuristic-Based Algorithms for Optimizing Fractional-Order Controllers—A Recent, Systematic, and Comprehensive Review. *Fractal Fract.* **2023**, *7*, 553. [CrossRef]
28. Ali, Z.M.; Ahmed, A.M.; Hasanien, H.M.; Aleem, S.H.E.A. Optimal Design of Fractional-Order PID Controllers for a Nonlinear AWS Wave Energy Converter Using Hybrid Jellyfish Search and Particle Swarm Optimization. *Fractal Fract.* **2024**, *8*, 6. [CrossRef]
29. Aldosary, A. Enhancing Microgrid Inverter-Integrated Charging Station Performance through Optimization of Fractional-Order PI Controller Using the One-to-One Sine Cosine Algorithm. *Fractal Fract.* **2024**, *8*, 139. [CrossRef]
30. Qin, H.; Kimball, J.W. Generalized Average Modeling of Dual Active Bridge DC–DC Converter. *IEEE Trans. Power Electron.* **2012**, *27*, 2078–2084. [CrossRef]
31. Mueller, J.A.; Kimball, J.W. An Improved Generalized Average Model of DC–DC Dual Active Bridge Converters. *IEEE Trans. Power Electron.* **2018**, *33*, 9975–9988. [CrossRef]
32. Shah, S.S.; Bhattacharya, S. Control of active component of current in dual active bridge converter. In Proceedings of the 2018 IEEE Applied Power Electronics Conference and Exposition (APEC), San Antonio, TX, USA, 4–8 March 2018; pp. 323–330. [CrossRef]
33. Micev, M.; Ćalasan, M.; Oliva, D. Fractional Order PID Controller Design for an AVR System Using Chaotic Yellow Saddle Goatfish Algorithm. *Mathematics* **2020**, *8*, 1182. [CrossRef]
34. Dulf, E.H. Simplified Fractional Order Controller Design Algorithm. *Mathematics* **2019**, *7*, 1166. [CrossRef]
35. Motorga, R.; Mureșan, V.; Ungureșan, M.L.; Abrudean, M.; Vălean, H.; Clitan, I. Artificial Intelligence in Fractional-Order Systems Approximation with High Performances: Application in Modelling of an Isotopic Separation Process. *Mathematics* **2022**, *10*, 1459. [CrossRef]
36. Zhao, W.; Wang, L.; Zhang, Z. Artificial ecosystem-based optimization: A novel nature-inspired meta-heuristic algorithm. *Neural Comput. Appl.* **2020**, *32*, 9383–9425. [CrossRef]

37. Menesy, A.S.; Sultan, H.M.; Korashy, A.; Banakhr, F.A.; Ashmawy, M.G.; Kamel, S. Effective parameter extraction of different polymer electrolyte membrane fuel cell stack models using a modified artificial ecosystem optimization algorithm. *IEEE Access* **2020**, *8*, 31892–31909. [CrossRef]
38. Zhao, W.; Zhang, Z.; Wang, L. Manta ray foraging optimization: An effective bio-inspired optimizer for engineering applications. *Eng. Appl. Artif. Intell.* **2020**, *87*, 103300. [CrossRef]
39. Hassan, M.H.; Kamel, S.; Salih, S.Q.; Khurshaid, T.; Ebeed, M. Developing chaotic artificial ecosystem-based optimization algorithm for combined economic emission dispatch. *IEEE Access* **2021**, *9*, 51146–51165. [CrossRef]
40. Ćalasan, M.; Jovanović, D.; Rubežić, V.; Mujović, S.; Đukanović, S. Estimation of single-diode and two-diode solar cell parameters by using a chaotic optimization approach. *Energies* **2019**, *12*, 4209. [CrossRef]
41. Arenas-Garcia, J.; Figueiras-Vidal, A.; Sayed, A. Mean-square performance of a convex combination of two adaptive filters. *IEEE Trans. Signal Process.* **2006**, *54*, 1078–1090. [CrossRef]

Disclaimer/Publisher's Note: The statements, opinions and data contained in all publications are solely those of the individual author(s) and contributor(s) and not of MDPI and/or the editor(s). MDPI and/or the editor(s) disclaim responsibility for any injury to people or property resulting from any ideas, methods, instructions or products referred to in the content.